Journal of Materials Chemistry A

ROYAL SOCIETY OF CHEMISTRY

PAPER

View Article Online
View Journal | View Issue

Cite this: J. Mater. Chem. A, 2025, 13, 40886

Photo-induced Raman amplification for detecting and monitoring degradation of micro- and nano-sized PVC plastics

Olugbenga Ayeni, [ab] Josiah N. Shondo, [cd] Tim Tjardts, [c] Sinan Şen, [e] Franz Faupel, [cf] Salih Veziroglu, [*cf] Oral C. Aktas [*ce] and Tayebeh Ameri [*afg]

The increasing environmental and health concerns posed by micro- and nanoplastics (MNPs) in various environmental matrices continue to call for urgent solutions. Given the inherent toxicity, persistence, bioaccumulation, and ability to absorb other pollutants, the development of highly sensitive catalytic materials and advanced analytical techniques for the detection and degradation of MNPs, particularly polyvinyl chloride (PVC-MNPs), in water and those originating from medical devices (MDs), is now of critical importance. Surface-enhanced Raman spectroscopy (SERS) shows potential for such detection; however, fabricating SERS-active substrates with hot spots and high sensitivity for detecting PVC-MNPs remains a challenge, necessitating advanced sensing approaches. In this study, we used a previously developed ultra-sensitive flower-like Ag nanoflake (Ag NF)-decorated TiO_2 platform with a high contact area alongside the photo-induced enhanced Raman spectroscopy (PIERS) technique under continuous UV irradiation for PVC-MNPs detection and degradation monitoring. The fabricated Ag NF-TiO_2 platform and PIERS approach facilitated the rapid detection of PVC particles down to 20 nm in water with a sensitivity increase of $\sim 2.6 \times 10^2$-fold over conventional SERS. The synergistic interplay between plasmonic effects and photo-induced charge transfer processes within the PIERS substrates significantly amplified the Raman signals of PVC-MNPs under UV irradiation. Furthermore, the PVC-MNPs loaded onto the Ag NF-decorated TiO_2 were photocatalytically degraded within 10 minutes of UV exposure. We proposed that photocatalytic-assisted dehydrochlorination and chain scission of PVC particles are the primary degradation mechanisms during the PIERS monitoring. The ultra-sensitive Ag NF-decorated TiO_2 platform and our innovative PIERS approach demonstrate significant potential for detecting and monitoring PVC-MNPs and can significantly advance the detection of MNPs in various environmental contexts.

Received 13th May 2025
Accepted 3rd August 2025

DOI: 10.1039/d5ta03860j

rsc.li/materials-a

1. Introduction

Polyvinyl chloride (PVC) plastic has increasingly been used industrially as a suitable material for construction and plumbing due to its strength, chemical resistance, and long lifespan.[1] In addition to these properties, its flexibility, biocompatibility, transparency, ease of sterilization, mechanical resistance, and low cost make it a suitable material for medical devices (MDs) such as intravenous (IV) bags, blood bags, catheters, infusion and dialysis tubes, feeding tubes, and endotracheal tubes.[2] However, when PVC is exposed to elevated temperature, UV light, gamma rays, or mechanical stress, it may undergo slow degradation. This degradation can lead to the fragmentation of PVC into small particles, such as microplastics (<5 mm) and nanoplastics (<1 μm), which contaminate drinking water from plumbing pipes and infused solutions from MDs.[3] The size of these micro- and nanoplastics (MNPs) renders them a severe threat to humans and patients.[4] Their size lets them penetrate many biological barriers in humans, and they can bioaccumulate, which can disrupt a cell's normal functioning.[5] This bioaccumulation, along with the environmental concern of PVC degradation, highlights the need for ongoing research to develop effective strategies for detection, monitoring, and degradation technologies, especially in processes like water

[a]Chair for Composite Materials, Department of Materials Science, Kiel University, Kaiserstr. 2, 24143 Kiel, Germany. E-mail: tam@tf.uni-kiel.de
[b]Department of Building, Ahmadu Bello University, Zaria, 810211 Kaduna, Nigeria
[c]Chair for Multicomponent Materials, Department of Materials Science, Kiel University, Kaiserstr. 2, 24143 Kiel, Germany. E-mail: sve@tf.uni-kiel.de; oca@tf.uni-kiel.de
[d]Department of Energy Conversion and Storage, Technical University of Denmark, 2800 Kgs Lyngby, Denmark
[e]Department of Orthodontics, University Hospital of Schleswig-Holstein (UKSH), Kiel University, Arnold-Heller-Straße 3, 24105 Kiel, Germany
[f]Kiel Nano, Surface and Interface Science KiNSIS, Kiel University, Christian Albrechts-Platz 4, 24118 Kiel, Germany
[g]Chemical Engineering, University of Edinburgh, Sanderson Building, Robert Stevenson Road, EH9 3FB Edinburgh, Scotland, UK

purification. As such, it is important to assess potable water and infusion solutions of MDs post-disinfection for any trace-level of PVC-MNPs.

PVC raises additional concerns due to the potential release of harmful additives like phthalates, bisphenol A (BPA), lead (Pb), cadmium (Cd), and organophosphates, and harmful chemicals like hydrochloric acid (HCl), arylamines, and dioxins throughout its lifecycle.[6,7] These additives can migrate from the matrix of PVC into drinking water or infused solutions of MDs, which further highlights the importance of evaluating the potential exposure risks of humans and patients to PVC-MNPs and their associated degradation products. The presence of PVC-based MNPs in drinking water sources can adversely affect not only the water quality but also have severe consequences on human health.[8,9] In addition, due to the prevalence of PVC-MNPs in MDs and their associated risks, there is a need to develop analytical and spectroscopic techniques capable of accurately detecting and quantifying PVC-rich MNPs as well as monitoring their degradation products at very low concentrations. However, achieving this level of sensitivity at low concentrations remains an unresolved challenge due to the sensitivity requirement for trace-level detection.[10] A robust analytical tool that is capable of accurately detecting and quantifying PVC-rich MNPs as well as monitoring their degradation products, is therefore needed. Such an analytical tool should be sensitive and specific enough to detect PVC-MNPs at very low concentrations.

Several analytical and spectroscopic techniques have been used to detect and monitor MNP pollutants.[11] Surface-enhanced Raman spectroscopy (SERS) has emerged as one of the most efficient and advanced analytical tools for monitoring environmental pollutants and toxins,[11,12] screening drugs and explosives,[13] forensic analysis of chemical and biochemical hazards,[14] and biomedical applications due to its high sensitivity, multiple detection capabilities, molecular specificity, portable instrumentation, and compactness. However, it still fails to meet the sensitivity requirements needed for trace-level detection of PVC NPs. This difficulty may be attributed to the intrinsic properties of PVC, which is a polar polymer with an asymmetric molecular structure.[15] As a result, the vibrational modes of PVC-MNPs may induce only minimal changes in molecular polarizability, which leads to a lower Raman cross-section.[16] Consequently, the SERS enhancement for PVC is limited, which complicates its sensitive detection.

While significant efforts are focused on improving SERS substrates through various techniques, SERS may not be the ultimate solution for PVC-MNPs detection. Hence, an alternative approach needs to be developed to detect PVC-MNPs and monitor their degradation products more practically. Based on previously reported studies, the photoactivation of SERS hybrid substrates (Au–TiO_2 and Ag–TiO_2), called photo-induced enhanced Raman spectroscopy (PIERS), may appear promising in the detection and degradation monitoring of PVC-MNPs.[17] The PIERS approach is based on pre- or co-irradiation of the hybrid substrate with UV light, which results in the enhancement of Raman signals beyond that of a conventional SERS substrate. PIERS approach has been typically used for the ultra-trace detection of explosives, pollutants, and biomolecules.[18,19] In this method, a PIERS substrate is pre-irradiated with UV light for a period of time before the loading of the analyte sample for Raman analysis, or it is irradiated after the analyte sample is loaded. As PIERS relies solely on UV irradiation, it streamlines the substrate preparation process and eliminates the need for additional steps.[20] The improved enhancement in Raman signals in PIERS is often attributed to the formation of oxygen vacancies (V_O) at the interface of the noble metal or metal-oxide semiconductor structure through the influence of UV light.[21] The formation of V_Os at the interface further enhances charge transfer between the photoexcited semiconductor, plasmonic particles, and adsorbed molecules and leads to a significant amplification of the Raman signal.[22] The creation of this V_O on the semiconductor surface is the widely accepted explanation of the PIERS effect.[23–25] Nonetheless, the synergetic effects of the hot electrons of plasmonic nanoparticles, the Schottky barrier at the metal and semiconductor interface, and the stability of V_O at this interface are critical factors that also contribute to the high enhancement factors (EFs) observed in PIERS.[26,27]

In a previous study, we demonstrated the PIERS effect using Rhodamine 6G (R6G $\approx 10^{-7}$ M) to compare the performance of PIERS and SERS on a 4N-in-1 hybrid substrate. The detection limit of the substrate was shown to extend down to 10^{-14} M.[27] In another study, we used the PIERS technique to investigate the dynamics of defective TiO_2 structures under ambient conditions, a feature that cannot be easily realized by vacuum-based techniques like TEM.[28] The study demonstrates how the PIERS technique can be used to probe the photoinduced surface oxygen vacancies and provide complementary insights into the behavior of these structures, expanding the application of PIERS beyond traditional uses. PIERS technology in combination with a coffee ring effect has also been reported capable of detecting microplastics of polystyrene (PS) at a trace level of 25, 28, 35, and 60 μg mL^{-1} in contaminated tap water, lake water, river water, and seawater, respectively.[29] While PIERS has been used for qualitative detection and monitoring of MNPs, its sensitivity and quantitative capabilities in detecting and monitoring PVC-MNPs and their degraded products at trace levels remain unexplored. The photo-induced charge transfer processes within PIERS substrates may enhance the amplification of Raman signals of PVC-MNPs, thereby offering an improved sensitivity compared to the conventional SERS technique. Furthermore, the use of PIERS in detecting PVC-MNPs can provide new insight into the safety of potable water for humans as well as the safety of MDs before they come directly in contact with patients. However, achieving enhanced sensitivity with PIERS for detecting trace levels of PVC-MNPs may require the development of highly sensitive catalytic materials and optimization of the PIERS detection process.

Furthermore, aside from the detection of MNPs at trace levels, there is also a growing interest in the scientific community to integrate photocatalytic materials with advanced tools to achieve both monitoring and degradation of MNPs, simultaneously. Recent studies have made significant advancements in the photocatalytic removal of MPs using TiO_2-

based or hybrid systems (TiO_2/ZnO), which are usually within suspended or slurry-phase reactors and under UV or solar irradiation.[30–32] These investigations have elucidated general pathways for reactive oxygen species (ROS)-mediated polymer degradation and discussed reactor designs, kinetic degradation profiles, and limitations of current technologies. Nonetheless, these systems are generally not reusable, prone to material agglomeration, and lack real-time monitoring of nanoscale plastic degradation activity as well as direct spectra capture of degradation intermediates, such as polyenes or dehydrochlorinated fragments. The lack of real-time monitoring is particularly critical, as the degradation of MNPs has been shown to be highly non-linear, often involving gradual structural transformation, which can lead to the formation and release of toxic intermediates or smaller, more persistent NPs, particularly under partial oxidation conditions.[33] Moreover, MNP degradation pathways can also change over time depending on environmental factors, which in turn affect the MNP release profiles at both molecular and microscopic levels.[34] Furthermore, current photocatalytic systems and techniques are limited by this unpredictability, as transient processes that influence treatment outcomes and environmental risk are frequently overlooked. In addition, studies have shown the importance of monitoring the abrupt release of harmful leachates, including phthalates, organochlorines, and HCl, particularly in the degradation of PVC-MNPs.[35] Related work has also revealed that the changing toxicity profiles of PVC degradation products are directly linked to specific degradation pathways that include backbone oxidation and dehydrochlorination.[36] All these findings reveal that post-degradation or endpoint analysis alone is insufficient to capture the key mechanistic and chemical transitions occurring during MNPs degradation. To this end, in this study, we propose an approach to address this gap using the PIERS technique under continuous UV irradiation, not only for enhanced detection of PVC-MNPs but also to monitor the *in situ* photocatalytic degradation of PVC-MNPs on a flower-like Ag nanoflake (Ag NF)-decorated TiO_2 platform. This dual-functionality approach provides both diagnostic and remediation capabilities, thereby expanding the role of plasmonic-semiconductor hybrid substrates in plastic pollution research.

In this study, by taking advantage of the enhanced sensitivity and potential selectivity of PIERS, we have demonstrated the applicability of an *in situ* diagnostic PIERS tool for detecting and analysing PVC-MNPs in water. Our research involved using the PIERS effect under continuous UV irradiation to detect and monitor the degradation of PVC-MNPs on flower-like Ag NF-TiO_2, which we developed earlier for photocatalytic clean-up of oil.[37] We also investigated the potential degradation mechanisms of these PVC particles during PIERS analysis. While a comprehensive solution to the global MNPs challenge remains elusive, our findings highlight that the ultra-sensitive Ag NF-decorated TiO_2 platform and our innovative PIERS approach demonstrate significant potential for detecting and monitoring PVC particles down to 20 nm. This innovative approach has the potential to significantly advance the monitoring of PVC-MNPs in various environmental matrices.

2. Experimental

2.1 Preparation of TiO_2 thin film

A custom-built vacuum deposition system with a DC planar magnetron source was used to deposit 500 nm thick TiO_2 thin films from a titanium target (Ti-Goodfellow, 99.99%, 50 mm diameter) on cleaned silicon (Si) and quartz substrates (10 mm × 10 mm) as previously reported.[27,38] The Si and Quartz substrates were transferred into the vacuum deposition chamber and a turbo molecular pump (Pfeiffer Vacuum, HiPace 400) in combination with ACP 15 roots pump (Pfeiffer Vacuum GmbH) was used to adjust the pressure in the chamber to a base pressure of 10^{-5} Pa. Argon (Ar) and oxygen (O_2) gas mixture set at an sccm ratio of 250 : 10 was supplied into the deposition chamber. The gas flow was controlled by mass flow controllers (MKS Multi-Gas Controller 674C) connected to two separate MKS Gas Controllers and the deposition was carried out at a magnetron power of 120 W. To ensure a homogenous thin film deposition, the Si and Quartz substrates on an automated sample holder were subjected to rotation. The TiO_2 thin films were deposited for 78 min. After the deposition process, the prepared TiO_2 thin films were annealed at 650 °C for 1 hour in an oven (Nabertherm LE 4/11/R6) and quenched in air immediately after the heat treatment. The heat treatment was carried out to induce nano-cracks in the thin films, thereby increasing the surface area of the TiO_2 structure. The Quartz substrates were used only to obtain the Raman signals of TiO_2 and TiO_2 samples loaded with PVC-MNPs. This was to minimize the influence of Si peaks.

2.2 Photocatalytic deposition of flower-like Ag on TiO_2 thin films

The synthesis reaction for the flower-like Ag nanoflakes (NFs) is shown in Scheme 1 (SI). Aqueous solution of silver nitrate ($AgNO_3$, Sigma-Aldrich, Germany) with a concentration of 3 mM was first prepared, as previously detailed.[37] A UV-transparent quartz cuvette was filled with 6.5 mL of the $AgNO_3$. Then, 100 μL of trisodium citrate ($Na_3C_6H_5O_7 \cdot 2H_2O$, Sigma-Aldrich, Germany) solution with a concentration of 0.4 M and 50 μL of Triton-X_{100} (Carl-Roth, Germany) were added to the solution. Using a universal pH indicator paper (MACHEREY-NAGEL), the pH of the solution was adjusted to 2 by adding tetramethylammonium hydroxide (TMAH) and nitric acid (HNO_3, Sigma-Aldrich, Germany). For each photocatalytic deposition of Ag NFs, the freshly prepared TiO_2 thin film sample on Si substrate was dipped into the quartz cuvette and irradiated for 10 min using a low-intensity UV light (UV LED StellarNet EPP2000C-SR-50 with SL5-DH light source) operating at a wavelength of 365 nm and a power of 4.5 mW cm^{-2}. Ag NFs structures were deposited on the prepared TiO_2 thin films by photocatalytic reduction of Ag^+ ions. Afterward, samples were rinsed with deionized water to remove excess solution and then allowed to dry at room temperature.

2.3 Synthesis of micro- and nano-sized PVC plastics

The PVC powder used for synthesizing the micro- and nano-sized PVC plastic in this study was purchased from Sigma-

Aldrich Company (Germany). The powder has an average molecular weight of 90 000 g mol^{-1} and a density of 1.4 g mL^{-1} at 25 °C, with particle sizes ranging from 105–250 μm (Fig. S1a, SI). Scheme 2 (SI) illustrates the synthesis procedure for the micro- and nano-sized PVC plastics, which is based on non-solvent induced phase separation (NIPS).[39] We used this approach to reduce the particle sizes of PVC powder to sizes below 5 μm. In a typical experiment, 44.4 mg of PVC powder was dissolved in 100 mL of Tetrahydrofuran (THF) to make a 0.05 wt% polymer solution and vigorously stirred for 60 min at room temperature. Subsequently, a solution containing 100 μL of potassium persulfate ($K_2S_2O_8$), 100 μL of sodium bicarbonate ($NaHCO_3$), 700 μL of deionized water, and 50 μL of polyethylene glycol (PEG) was prepared separately as an aqueous solution. Afterwards, 50 μL was drawn from the 0.05 wt% polymer solution and added dropwise into the water-based solution to induce precipitation of PVC particles. This was done under continuous ultrasonication for 6 min to prevent PVC particle agglomeration. The resulting precipitate was washed and filtered through a series of filter membranes to obtain different PVC particle sizes: 20 nm (Whatman™ Anotop™ 25 syringe filter) and 200 nm, 450 nm (Whatman™ Puradisc™ 25 polytetrafluoroethylene syringe filter), and 5 μm (Whatman™ Puradisc™ 13 polytetrafluoroethylene syringe filter). The mass concentration of the PVC particles in the aqueous solution was 22.2 μg mL^{-1} and was fixed throughout the experiment. As the concentration of PVC particles in the aqueous solution was fixed, the filtration step was used to separate PVC particles into distinct size ranges for further detection on the Ag–TiO_2 substrates using the SERS and PIERS approach. The synthesized PVC is shown in Fig. S1b, SI.

2.4 Characterization of PVC, Ag–TiO_2, and PVC/Ag–TiO_2

The surface morphology of synthesized PVC particles, prepared Ag–TiO_2 substrates, and Ag–TiO_2 substrates loaded with PVC particles (PVC/Ag–TiO_2) was investigated using a scanning electron microscope (SEM) from Zeiss (Supra55VP-Carl) operating under an acceleration voltage of 3 kV and a standard aperture size of 30 μm. To investigate the chemical composition of the Ag–TiO_2 and PVC/Ag–TiO_2 sample surface, X-ray photoelectron spectroscopy (XPS, XPS UHV system from PREVAC Sp. z o. o., Al-anode, 300 W) was utilized. Survey scans were conducted at 3 iterations and a pass energy of 200 eV, while high-resolution scans were performed at 20 iterations and a pass energy of 50 eV. CasaXPS software (version 2.3.23) was used for the analysis of XPS spectra. The background of each spectrum was quantified by applying the Shirley algorithm. The charge correction was done by fitting the Ag 3d main peak and setting the peak position of the fit to 368.1 eV while adjusting all belonging spectra accordingly. In addition, the atomic percentages (at%) of elements were extracted from the wide scan data after carefully integrating the relevant elemental peaks. Furthermore, the surface wetting properties of the Ag–TiO_2 samples were investigated using a semiautomated contact angle goniometer (OCA 30, Dataphysics). For static water contact angle (WCA) measurements, water droplets with a volume of 10 μL were used. X-ray diffraction (XRD) measurements were conducted on the prepared Ag–TiO_2 samples using a Rigaku SmartLab system with a 9 kW rotating Cu anode X-ray source ($\lambda \approx 1.54$ Å). The measurement was set up in a grazing incidence XRD configuration with an omega (ω) angle of 4°. Scans were performed at a rate of 4° min^{-1} with a step size of 0.04°, and the instrument operated at 45 kV and 200 mA.

2.5 Raman measurement

Raman spectroscopy was performed using a confocal Raman spectrometer (WITEC alpha300 RA, Ulm, Germany) equipped with a Nd:YAG laser beam ($\lambda = 532$ nm with 40 mW of power). The Raman spectra of TiO_2 prepared on quartz substrate and that of TiO_2 samples loaded with PVC-MNPs were acquired using an ×100 microscope objective lens with 0.90 numerical aperture (NA), while Ag–TiO_2 samples prepared on Si substrates for SERS and PIERS measurements were acquired using an ×50 microscope objective lens with a 0.55 NA. A diffraction grating density of 600 g per mm BLZ was employed for all spectra acquisition. Raman mapping was performed with 250 × 250 lines over a 50 × 50 μm area for the Ag–TiO_2 substrate. For all Raman, SERS, and PIERS signal acquisition, a fixed volume of 10 μL of the PVC analyte solution (*ca.* 22.2 μg mL^{-1}) was drop-cast on the surface of prepared TiO_2 and flower-like Ag NF–TiO_2 substrates. The analyte was allowed to dry naturally for 30 min at room temperature. The integration time for the PVC analyte was set to 30 s. The final spectrum was obtained after baseline correction. SERS measurements were performed on non-irradiated substrates.

For all PIERS spectra acquisition, the prepared substrate was first preirradiated with a UV source of 365 nm for 20 min, and the PVC analyte solution was drop-cast on the preirradiated samples and allowed to dry for 30 min at room temperature. For the detection of PVC-MNPs, the Ag–TiO_2 substrate was irradiated with UV after the drying process, and PIERS signals were acquired afterwards. For each PIERS signal acquisition, the laser dwelling time was 30 s. Furthermore, to monitor the degradation of PVC-MNPs under UV light, PIERS signals were acquired at cumulative time intervals of 10 min, 20 min, and 30 min. For each of these time durations of PIERS signal acquisition, the laser dwelling time was fixed at only 30 s. The acquired PIERS signals allowed for monitoring changes in the PVC backbone over these periods. The diameter of the laser spot on the sample surface was about 1 μm. The UV light was positioned to irradiate the substrate from the side at a fixed distance of 5 mm. Three batches of similarly prepared Ag–TiO_2 substrates were used to ensure reproducibility in the degradation trends. As a reference, Raman measurement of the original PVC powder was performed, and the corresponding peak positions are shown in Fig. S2. Furthermore, the Raman spectrum of the TiO_2 and its corresponding bands are shown in Fig. S3.

3. Results and discussion

3.1 Substrate characterization

Fig. 1a and b show the surface morphology of the photo-deposited Ag NFs with flower-like structures on a TiO_2 thin film.

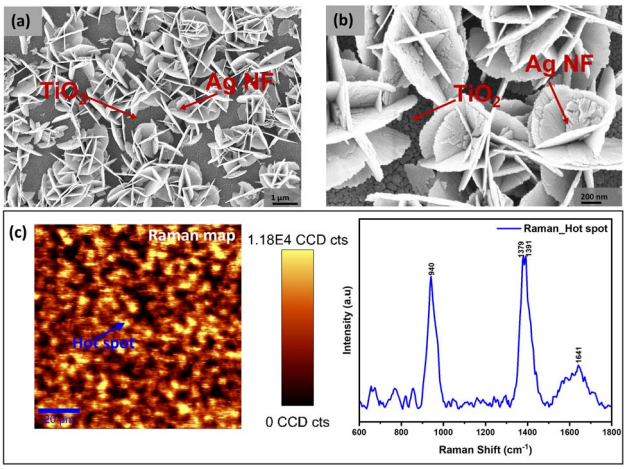

Fig. 1 SEM image of Ag NFs on TiO_2 thin film at (a) low magnification and (b) high magnification. (c) Raman map of Ag NFs with corresponding normal Raman spectra of the Ag–TiO_2 hot spot region.

As we previously demonstrated, we hypothesize that the initial photoexcited charge carriers generated by TiO_2 triggered the photooxidation of citrate ($C_6H_5O_7$) ions in the $Na_3C_6H_5O_7$, which was the reducing agent used in this study, leading to its decarboxylation into organic radicals.[37] These radicals are then chemisorbed onto Ag^+ ions through electron transfer, ultimately resulting in the reduction of Ag^+ ions to form stable metallic Ag structures immobilized on the TiO_2 surface (Scheme 1, SI). The Raman map of the substrate reveals regions of hot spots within the Ag NF structure. These hot spots are localized between two Ag nanoplates, with the corresponding Raman spectra shown in Fig. 1c. We expect these hot spots, which are regions of high electromagnetic field within the Ag NFs structure, to play a key role in achieving much stronger Raman signals, which will enable the effective detection of PVC-MNPs through PIERS.[40] The observed intense peaks at 940 cm^{-1}, 1379 cm^{-1}, and 1385 cm^{-1} are due to the citrate ion chemisorbed vibrational modes on the Ag nanostructures' surface (Fig. 1c).[41]

The peak at 940 cm^{-1} is attributed to symmetric vibration ν_s(C–C) in the citrate ion, while the peaks at 1379 cm^{-1} and 1385 cm^{-1} are assigned to $\nu_s(COO^-)$ mode in the citrate ion.[42] The broad defective peak at 1641 cm^{-1}, which is less prominent than the observed $\nu_s(COO^-)$ peak, is associated with asymmetric vibration $\nu_{as}(COO^-)$ mode of the carboxylate group. In order to remove the chemisorbed citrate molecules and avoid misinterpretation of Raman peaks during SERS and PIERS analysis, the Ag–TiO_2 substrates were further annealed at 200 °C for 30 min, as shown in the Raman spectrum of Fig. S4a. After the annealing process, no structural difference in the XRD pattern of annealed Ag–TiO_2 is observed (Fig. S4b). Additionally, the surface wetting property of the Ag–TiO_2 substrate is shown in Fig. S5. Before the pre-irradiation of the substrate with UV light, it was observed to be hydrophobic with a WCA of 91° ± 1. However, post-UV irradiation made the surface hydrophilic (WCA = 6° ± 1). The change in the wetting behavior of the substrate is attributed to the surface energy difference.[43]

3.2 PVC interaction with Ag NFs

The surface morphology and spatial distribution of PVC particles interacting with Ag NFs are shown in Fig. 2a and b. We observed attachment and relatively large contact areas of PVC-MNPs on the Ag NFs. This might be due to the flake-like morphology facilitating this attachment. Some PVC particles were seen attached to the tips of the Ag NFs, while others were in between two Ag nanoplates. Fig. 2c presents a schematic of potential interactions between PVC particles and Ag NFs surfaces and tips. The schematic suggests local interaction, likely governed by electrostatic or van der Waals forces.[44] Due to this configuration, more contact might lead to an increase in charge transfer, and we expect that this will enhance the sensitivity and specificity of PIERS for detecting PVC particles. Further interactions may be influenced by the roughness of the Ag NFs, resulting in multiple sites for the adhesion of PVC particles. Moreover, if the PVC particles are located between two Ag nanoplates, they can be subject to a 'hot spot' effect, in which the localized electromagnetic field is significantly enhanced, thus increasing the PIERS signal.[45]

We further confirmed the presence of PVC on the Ag NFs substrate by XPS analysis (Fig. 2d). The XPS spectrum of the Cl 2p of the Ag–TiO_2 sample loaded with PVC reveals the presence of PVC particles on the substrate. In addition to the Cl 2p peak, other peaks associated with the Ag–TiO_2 substrate, such as Ag 3d, C 1s, O 1s, and Ti 2p, were also observed, similar to our previous work.[27] Significantly, the result shows that the chemical presence of PVC on the Ag NFs was consistent with what we observed during SEM analysis.

3.3 PIERS mechanism

In our study, we detected and monitored the degradation of PVC-MNPs *via* PIERS under continuous UV irradiation after substrate pre-irradiation. The continuous irradiation of our

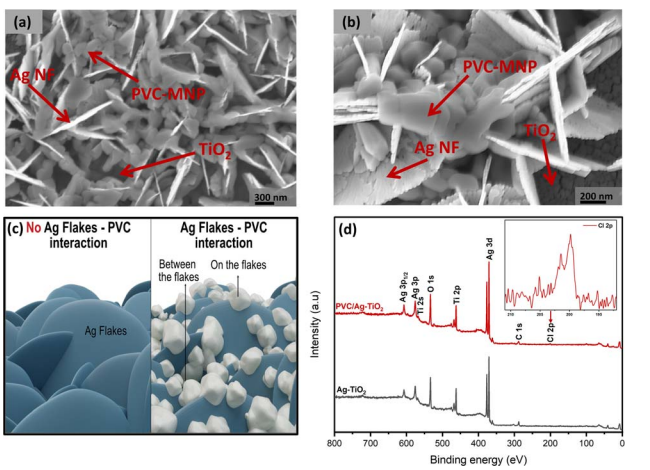

Fig. 2 SEM image of PVC-MNPs loaded on Ag–TiO_2 thin film at (a) low magnification and (b) high magnification. (c) Schematic depiction of the interaction of PVC-MNPs with Ag NFs, and (d) XPS analysis of pristine Ag–TiO_2 and Ag–TiO_2 loaded with PVC-MNPs with insets of Cl 2p.

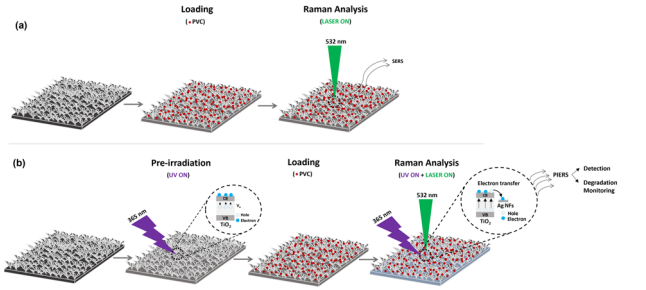

Fig. 3 Schematic of (a) SERS detection of PVC-MNPs on Ag–TiO_2 platform and (b) PIERS detection and degradation monitoring of PVC-MNPs on Ag–TiO_2 platform. For each PIERS signal acquisition during Raman analysis, laser (λ = 532 nm with 40 mW of power) was on for only 30 s and for degradation monitoring of PVC-MNPs, PIERS signals were acquired at cumulative time intervals of 10 min, 20 min, and 30 min of UV on.

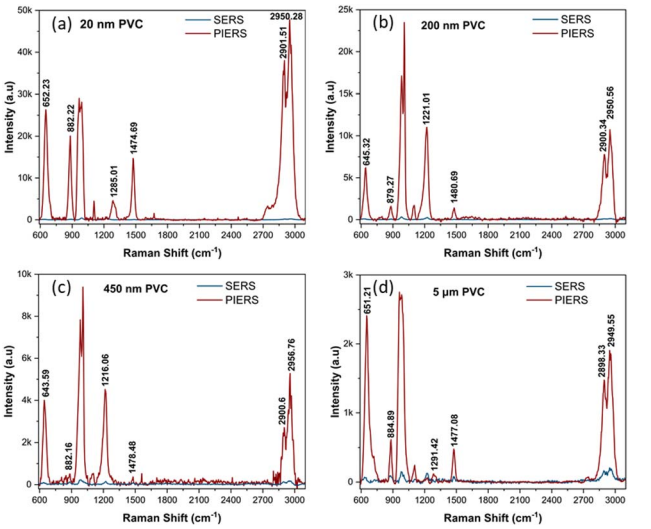

Fig. 4 Comparison of Raman signal intensity of SERS and PIERS in the detection of (a) 20 nm PVC, (b) 200 nm PVC, (c) 450 nm PVC, and (d) 5 μm PVC, with different y-axis scales.

SERS-sensitive Ag–TiO_2 substrate with UV allowed us to detect PVC-MNPs on one hand and, on the other hand, monitor the degradation taking place in the PVC during Raman analysis (Fig. 3).

We believe that, in addition to the creation of V_O defects in the Ag–TiO_2 semiconductor substrate, continuous UV excitation generates charge carriers for immediate interaction with Ag NFs and PVC NPs.[25] Consequently, continuous UV irradiation can also increase the PIERS relaxation time and ensure a steady electron transfer from TiO_2 to Ag NFs, hence increasing the electron density of the Ag NFs.[46,47] Additionally, continuous UV irradiation can cause adsorbed PVC molecules on the Ag NFs to undergo some photochemical modifications and promote the formation of reactive polyene species with a backbone of alternating single (C–C) and double (C=C) bonds.[48] These reactive species are formed in PVC as a result of the dehydrochlorination taking place in PVC under the influence of UV irradiation.[49] As a result, any chemical transformations or intermediates generated by the UV-activated TiO_2 are immediately subjected to laser-induced Raman excitation, making the detection and degradation monitoring of PVC-MNPs possible.

3.4 SERS and PIERS detection of micro- and nano-sized PVC plastics

Fig. 4 shows the SERS and PIERS signals of the different PVC-MNPs analyzed in this study. The peak around 600–700 cm^{-1} and 850–900 cm^{-1} is attributed to the stretching vibrations of C–Cl bonds, the peak around 1200–1300 cm^{-1} is assigned to C–H in-plane bending vibrations, while the peak around 2750–3100 cm^{-1} is associated with the asymmetric CH_2 stretching vibrations.[50] Comparing the intensities of the SERS and PIERS spectra, it is clear that remarkable enhancement of Raman signals can be achieved with PIERS *via* UV excitation. In comparison with Raman signals, both SERS and PIERS exhibited a significant enhancement in Raman signal, as shown in Fig. S5 and S6 (SI). Given the weak Raman signal from both Raman and SERS, we assumed that induced V_O effects were present after exposing the substrate to UV, resulting in the observed enhancement in PIERS compared to SERS.[51] For the PIERS spectra of the different PVC particles, we observed that as the size of the PVC plastic reduces, the PIERS signal undergoes a continuous enhancement, with a significant increase in the Raman intensity of the 20 nm PVC plastic in the order of ~2.6 × 10^2-fold enhancement over conventional SERS (peak around 600–700 cm^{-1}). The respective enhancement factors (EFs) for the different sizes of PVC particles are presented in Table S1(a–d).

The observed size-dependent enhancement trend in the PIERS signals over SERS can be explained by the spatial relationship between the Ag NF–TiO_2 substrate and the laser spot, as well as the ability of the particles to interact with plasmonic hotspots. The lateral diameter of the laser spot in our Raman setup was calculated to be ~1.18 μm (using 1.22λ/NA).[52] This spot size fully encompasses the smaller PVC particles (20 nm), allowing efficient excitation and interaction with the enhanced near-field regions on the substrate. In contrast, larger particles (5 μm) significantly exceed the spot size, resulting in partial illumination, where only a fraction of the particle is excited. This reduces the effective scattering volume and overall signal intensity. Previous reports,[53] have demonstrated that nanoplastics outside the center of the laser spot generate notably weaker signals due to limited excitation, emphasizing how particle positioning relative to the laser spot can affect spectral output. In addition, smaller PVC particles possess a higher surface-area-to-volume ratio, which enables more extensive interaction with the plasmonic hotspots generated by the Ag NFs on TiO_2. These particles can more readily nestle within the nanoscale enhancement zones, leading to stronger field confinement and signal amplification. In contrast, larger particles are less likely to conform to or reside within these nanoscale hotspots due to geometric constraints, which limit their enhancement efficiency. These two effects explain why the PIERS enhancement relative to SERS is much stronger for

nanoscale PVC particles (20 nm), while this difference becomes less pronounced for microscale particles (5 μm), which suffer from reduced hotspot compatibility and incomplete excitation coverage. In addition, Fig. S8 illustrates consistent PIERS signals recorded from different positions across the Ag–TiO_2 substrate loaded with 20 nm PVC-MNPs. The uniformity in signal intensities across multiple regions highlights the reproducibility of the enhancement and the spatial homogeneity of hotspot distribution on our substrate.

Alongside comparing our PIERS-based methodology with conventional SERS, we further evaluated the impact of continuous UV irradiation during Raman acquisition, which constitutes the principal difference in our technique in relation to the conventional PIERS. While conventional PIERS configurations typically involve only UV pre-treatment of the plasmonic-photocatalyst surface, our results demonstrate that maintaining continuous UV exposure throughout spectral acquisition significantly enhances the intensity of characteristic PVC bands. As shown in Fig. S9 (SI), the PIERS spectra obtained under continuous UV exhibit stronger signal intensity across key vibrational modes of PVC, compared to the spectrum from conventional PIERS using the same Ag NF–TiO_2 substrate. This enhancement we attributed to the sustained generation of photogenerated charge carriers and the dynamic plasmon-photocatalytic interactions under continuous UV irradiation.[54] This likely amplified the molecular interactions and signal acquisition during measurement. Taken together, the improved signal intensity highlights the advantages of integrating continuous UV within our PIERS detection scheme. In addition, we compared our PIERS-based approach against recent techniques used for the detection of MNPs, including PIERS, SERS, fluorescence staining, and NEMS-FTIR spectroscopy. As summarized in Table S2 (SI), our method is promising in terms of the detection limit of PVC (20 nm), *in situ* operation, and cost-effectiveness, in addition to the simplicity of the Ag NF-TiO_2 platform fabrication. Also, due to the surface-immobilized configuration of the Ag NF-TiO_2 substrate, our photocatalyst platform offers the potential for long-term degradation reusability compared with conventional single-use SERS substrates.

Furthermore, in addition to detecting the main peaks of PVC *via* our approach, we also observed the degradation products of PVC, specifically polyenes, around 1100–1110 cm^{-1} and 1475–1480 cm^{-1} (Fig. 4). We believe that our highly active and ultrasensitive photocatalytic Ag–TiO_2 substrate facilitated the rapid detection of these degradation products under continuous UV exposure.

3.5 PIERS monitoring of micro- and nano-sized PVC plastic degradation

Using PIERS, we monitored the molecular structure and chemical changes in PVC-MNPs exposed to continuous UV irradiation for 10 minutes. Fig. 5a–d shows the PIERS-based monitoring of the degradation of PVC particles of different sizes on the photocatalytic Ag–TiO_2 substrate. As the PVC-MNPs undergo photo-degradation, we observed some changes in the fingerprint of the PVC plastics in the range 600–1800 cm^{-1} and high wave number range of 2750–3100 cm^{-1}. In principle, the different transformations and changes occurring in the different PVC particles under continuous UV irradiation can be associated with changes in peak intensities, broadening of peaks, formation of new peaks, or disappearance of the existing peaks. More so, as the PVC-MNPs get irradiated with UV light, different chemical reactions like chain scission, oxidation, and dehydrochlorination can occur within the material.[55] These reactions can alter the vibrational modes of the polymer's molecular bonds and may result in the formation of polyenes or carbonyls within the polymer backbone. The nature and extent of these reactions can be influenced by UV intensity, duration of UV exposure, photocatalytic material in use, temperature, availability of oxygen, chemical environment, mechanical stress, additives, stabilizers, surface area, and particle size.[48,49]

Interestingly, from Fig. 5a–d, we observed a significant decrease in peak intensity of the C–Cl stretching vibration peak of PVC in the range 600–700 cm^{-1} and CH_2 stretching vibration in the range 2750–3100 cm^{-1} after continuous UV exposure for 10 min. For instance, for PVC particles in the 20 nm range, the decrease in Raman intensity of the C–Cl stretching vibration peak is about 99.8% while for particles in the 5 μm range, it is 99.7%. The observed decrease in the Raman intensity of the 600–700 cm^{-1} C–Cl stretching vibration peak range indicates the dehydrochlorination process in the PVC polymer backbone.[48] Structural changes in the PVC polymer backbone were also visible as revealed by the broadening of the peak around 800–900 cm^{-1} which corresponds to C–Cl wagging vibrations.[48] A reduction in the 1400–1500 cm^{-1} peaks associated with C=C stretching vibrations was also significant. The breaking of the C–C bond further complements the degradation in the PVC. Though we expected that as the dehydrochlorination process is taking place in the PVC-MNPs, the peaks of the earlier detected polyenes in the region of 1100–1110 cm^{-1} and 1475–1480 cm^{-1}, which are characteristic of C–C stretching vibration and C=C stretching vibration,[48] respectively, would become more

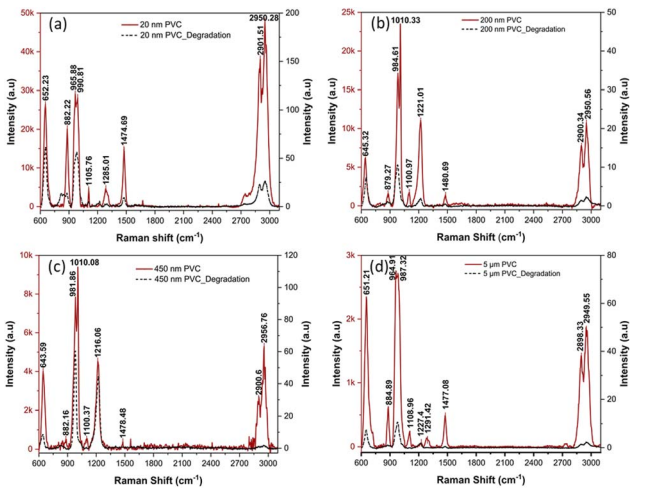

Fig. 5 PIERS monitoring of the degradation of PVC-MNPs after 10 min of UV irradiation (a) 20 nm PVC, (b) 200 nm PVC, (c) 450 nm PVC, and (d) 5 μm PVC, with different *y*-axis scales.

intense. This is because, as HCl is continuously eliminated from the PVC backbone, it should facilitate the formation of high concentrations of long-conjugated polyenes, thus enhancing the intensity of their corresponding vibrational modes.[48,56] On the contrary, the intensity of these peaks further decreased as observed in the Raman spectra upon continuous UV exposure. Instead of the formation of long conjugated polyene sequences, short non-conjugated polyenes (unstable polyenes) with weak Raman signals might have been formed during the photo-degradation process, making their detection difficult by PIERS.[57]

Moreover, the absence of a distinct carbonyl (C=O) peak may therefore reflect a low concentration of the C=O species below the Raman detection threshold of our system, early-stage degradation dominated by dehydrochlorination, or potential suppression of the Raman signal due to reduced surface accessibility caused by MNP coverage on the substrate.[58] This is consistent with reported pathways under non-thermal, photo-chemically driven conditions, where oxygenated species, such as ketones or aldehydes, may form more gradually or in minor amounts.[59] In addition, the unobserved C=O species in our PIERS spectra, can be attributed, on one hand, to the short UV irradiation times (10–30 min) applied to the PVC-MNPs, and on the other hand, to the presence of polyethylene glycol (PEG) used in the synthesis of the PVC-MNPs, which is known to moderate the extent of photooxidation. Specifically, PEG can scavenge free radicals or alter oxygen accessibility at the polymer-surface interface, thereby suppressing the formation of carbonyl functionalities. Similar suppression of C=O formation has been reported in PVC systems containing stabilizing additives and complexes.[60] The behavior observed in our PIERS spectra is consistent with this study, where additive-blended polymers exhibited reduced oxidative degradation even under UV exposure. However, the chain scission in the CH_2 stretching vibration bond around 2750–3100 cm^{-1} further reaffirms that degradation is taking place in the PVC.[15] In this range, we observed some peak broadening and changes in intensities which is indicative of the breaking of the C–H bond in the polymer backbone.[61] The observed peak broadening in this region may be due to the local chemical environment around hydrogen atoms due to structural changes.

Fig. S10 further reveals the PIERS spectra related to the degradation taking place over different time durations (10, 20, and 30 min) in the various PVC particles. Most significant is the total elimination of the CH_2 stretching vibration of the PVC backbone around 2750–3100 cm^{-1} after 30 min of UV exposure. However, the apparent increase in the C–Cl stretching signal observed around 600–700 cm^{-1} in Fig. S10b and S10d is attributed to the overlapping background peak of the E_g lattice vibrational mode of anatase TiO_2 as shown in the normal Raman spectra of Fig. S3 and also in the annealed Ag–TiO_2 NFs (Fig. S4a). This overlap signifies further decomposition of PVC and the subsequent exposure of the underlying substrate. Furthermore, to demonstrate the reproducibility of the degradation trend, we show in Fig. S11 the 10 min degradation trend across 3 batches of our Ag–TiO_2 platform loaded with 20 nm PVC particles.

To further elucidate the degradation taking place in the PVC-MNPs being detected and monitored *via* PIERS, we conducted an XPS analysis. Fig. 6a shows the XPS survey scans of the Ag–TiO_2 substrate without nano-PVC particles, the substrate loaded with nano-PVC particles before degradation and after 10 min and 30 min degradation. The XPS spectrum reveal the changes in surface composition due to the degradation process. Fig. 6b shows the Cl 2p binding energy region and the presence of a Cl 2p peak on the surface of the Ag–TiO_2 substrate loaded with 20 nm before exposure to UV light. After 10 min of UV exposure, the Cl 2p peak on the substrate loaded with 20 nm PVC particles was not visible indicating that degradation of nano- PVC particles was taking place on the Ag–TiO_2 substrate. With further exposure of the substrate to UV light for 30 min, the Cl 2p was still not visible on the surface, further confirming the degradation of the nano- PVC particles. Fig. 6c and d shows the atomic percentages of C and Cl extracted from the integration of all elemental peaks in the XPS spectrum plotted on the C 1s peak. Before degradation, the Ag–TiO_2 substrate showed ~16 at% C and ~3 at% Cl and ~7 at% C after 30 min of degradation. The non-presence of Cl and the lower percentage of C on the substrate after the degradation process further suggest that dehydrochlorination and chain scission took place in the PVC backbone. We further analyzed the degradation of other PVC particle sizes on the Ag–TiO_2 substrate and observed that the Cl 2p was not visible after the degradation process in all the samples after 30 min of UV exposure (Fig. S12).

These XPS findings were further supported by attenuated total reflectance Fourier transform infrared spectroscopy (ATR-FTIR) analysis as shown in Fig. S13. The C–Cl stretching band in the 600–700 cm^{-1} region shows a decrease after 10 and 30 minutes of UV irradiation, which indicates the dehydrochlorination of PVC. The reduction in the C–Cl vibrational mode further supports the XPS observations, which show a decrease in the Cl 2p intensity. In addition, we observed a subtle broadening around the 850 cm^{-1} peak for samples loaded with 20 nm PVC

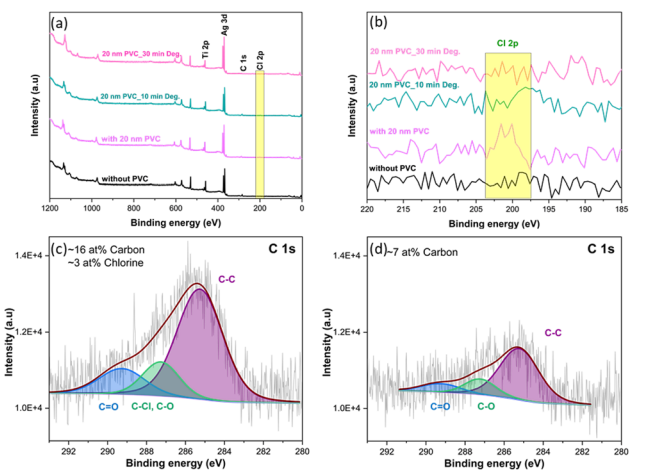

Fig. 6 XPS analysis of (a) 20 nm PVC degradation, (b) corresponding Cl 2p peak of 20 nm PVC, (c) C 1s peak of 20 nm PVC degradation before degradation, and (d) C 1s peak of 20 nm PVC degradation after 30 min degradation.

and irradiated with UV for 10 and 30 min. This may be associated with increased molecular disorder or backbone rearrangements within the PVC matrix, which is consistent with the early stages of photodegradation.[62] This change also supports the chemical transformations occurring in the PVC matrix.

In addition to monitoring the PIERS signal for degradation assessment, we examined the morphological stability of the Ag–TiO_2 substrate after UV exposure (30 min). The SEM images in Fig. S14 reveal morphological changes in the Ag nanostructures, including rounding and partial coalescence, which are characteristic of plasmon-induced reshaping. These transformations are commonly reported for silver-based plasmonic systems under prolonged UV irradiation and are attributed to local heating and surface diffusion effects.[63–66] Despite these morphological changes, the PIERS signal across the different time domains analyzed (Fig. S10) can still be acquired, distinct from the Raman spectra of the annealed Ag NF–TiO_2 substrate in Fig. S4a. This demonstrates that the substrate retains its functionality under UV exposure conditions relevant to this study. These findings also provide valuable insights into the dynamic behavior of the Ag NFs under UV irradiation and suggest opportunities for further optimization in future work. Strategies such as surface passivation of the Ag NFs may help further enhance long-term stability for extended UV irradiation or repeated use. Moreover, while reusability was not investigated in this study, our previous work showed that a comparable Ag-based 4N-in-1 hybrid substrate maintained consistent PIERS enhancement over at least 18 cycles, using Rhodamine 6G (R6G, $\sim 10^{-7}$ M) as a model analyte, without significant loss of plasmonic or photocatalytic performance, further supporting the potential for repeated use.[27]

3.6 Proposed degradation mechanism of micro- and nano-sized PVC plastics

In the previous section, we have focused on the PIERS spectra of PV-MNPs acquired under continuous UV light illumination upon measurement. The decrease in Raman peak intensity already occurring after 10 min of UV exposure, we attributed to dehydrochlorination. Furthermore, the occurrence of broadening of peaks, we associated to structural changes due to chain scission. While prior studies have outlined general mechanisms for plastic degradation under photocatalysis, particularly ROS-mediated oxidation and dehydrochlorination, these studies have largely focused on bulk polymers or suspended catalysts.[67,68] Moreover, recent advances have broadened the understanding of the kinetic degradation of plastics, reactor designs, and the performance of TiO_2-based or heterostructured photocatalysts for MPs removal.[30,31] However, these studies still emphasize post-analysis of degradation or bulk treatment setups, with limited attention to real-time degradation tracking or sensitivity to nano-sized particles. In contrast, our approach utilizes an Ag NF-TiO_2 platform that not only catalyzes the degradation of PVC-MNPs but also allows *in situ* Raman tracking of the PVC matrix during degradation. Interestingly, we observed measurable Raman spectral changes within 10 to 30 minutes of UV exposure, including decreased intensities of C–Cl and C–H bonds, as well as the formation of conjugated polyene structures. This highlights our platform's capability for real-time mechanistic insight at the nanoscale, which remains largely underexplored. Moreover, as the exact mechanism of PVC degradation under various environments and experimental conditions is not fully understood, several well-established pathways exist. Building on this, we propose that, in the presence of Ag–TiO_2, the degradation of PVC-MNPs under continuous UV irradiation primarily occurs through two mechanisms: photocatalytic-assisted dehydrochlorination and photocatalytic-assisted chain scission. Fig. 7 shows a schematic summary of the photocatalytic processes at the Ag–TiO_2 site and the two proposed photocatalytic-assisted degradation mechanisms under continuous UV irradiation.

Based on our observations from the MNPs degradation during PIERS analysis, we propose that both UV light and visible light contribute to this process. First, as the Ag–TiO_2 substrate loaded with PVC particles gets exposed to UV light, the TiO_2 semiconductor absorbs photons and generates electron–hole pairs, which interact with adsorbed O_2 and water molecules on the TiO_2 surface. The electrons generated reduce the adsorbed O_2 to superoxide anions ($O_2^{\bullet -}$) and the holes oxidize the adsorbed water to hydroxyl radicals ($OH^{\bullet}$).[69] The ROS, such as $OH^{\bullet}$, then react with the PVC-MNPs. While TiO_2 is the primary driver of the degradation process, the plasmonic material, which in our study is Ag NFs, also plays a key role by acting as electron trapping centers, which can enhance electron transfer and photocatalytic degradation efficiency.[69]

Due to the high reactivity of the $OH^{\bullet}$ ROS, they can readily attack the PVC polymer chain. This attack on the polymer chain results in the dehydrochlorination of the C–Cl peak and chain scission of the C–C and C–H bonds. The $OH^{\bullet}$ radical weakens the C–Cl bonds in the PVC polymer structure as hydrogen atoms are abstracted from the PVC chain. The removal of these hydrogen atoms from the carbon atoms adjacent to the chlorine atoms initiates the dehydrochlorination process, causing the loss of chlorine as HCl acid. As the C–Cl bond breaks, HCl is released with a carbon radical left in the PVC backbone. As the dehydrochlorination process progresses, this carbon radical further reacts with adjacent Cl atoms, leading to more dehydrochlorination in the PVC polymer chain.

In addition to the dehydrochlorination, concurrently, chain scission is also promoted by the $OH^{\bullet}$ radical. As the $OH^{\bullet}$ radical interacts with the PVC polymer, fragmentation of the polymer chain occurs, and this leads to changes in the structure of the polymer. In our study, the observed reduction in the Raman peaks associated with the C–C around 1400–1500 cm^{-1} and C–H

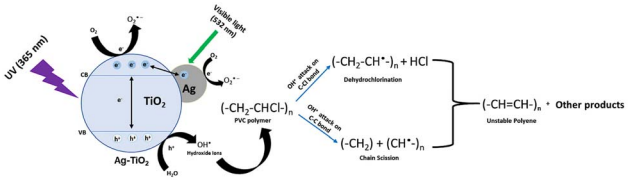

Fig. 7 Proposed photocatalytic degradation mechanism of micro- and nano-sized PVC plastics during PIERS analysis.

bonds in the range 2750–3100 cm^{-1} of the PVC polymer backbone suggests that the PVC-MNPs polymer chains have become shortened and are now less ordered. The dehydrochlorination and chain scission process produces smaller fragments of the PVC polymer and the ROS attack on the polymer chain continues until no polymer is left on the Ag–TiO_2 substrate or ceases when the photocatalyst becomes less effective. More so, we believe that the dehydrochlorination and chain scission of the PVC-MNPs were further accelerated by the presence of Ag NFs on the TiO_2 semiconductor. The plasmonic Ag metal can enhance the local electromagnetic field around organic pollutants *via* surface plasmon resonance (SPR), which, in turn, can facilitate the generation of hot electrons and ROS under UV irradiation. These species can actively participate in breaking bonds in the PVC chains, thereby promoting degradation. We believe that the synergetic effect of the TiO_2 photocatalyst and the SPR effect of the Ag NFs might have contributed to the observed degradation in our study.

4. Conclusions

In conclusion, we demonstrated the use of a PIERS technique for the detection of PVC plastics down to 20 nm size with high sensitivity under continuous UV irradiation. This PIERS approach allows the monitoring of the photocatalytic degradation of micro- and nano-sized PVC plastics exposed to UV light, revealing their corresponding degradation dynamics over an irradiation period. In addition, we showed that the nanostructure of our ultra-sensitive flower-like Ag NF-decorated TiO_2 platform played a crucial role in enhancing the interaction with nano-sized PVC particles, as demonstrated by SEM images. The nanostructure of Ag NF also facilitated the detection and degradation monitoring of PVC-MNPs *via* PIERS under continuous UV illumination. This study advances the application of PIERS in environmental detection as well as provides valuable insight into the degradation mechanisms of PVC-MNPs. The findings of this study have important implications for the development of sensitive detection methods for MNP pollutants in the environment, enhancing environmental monitoring and water purification strategies. Furthermore, the PIERS-based approach used in this study may pave the way for improving the efficiency of the PIERS technique, making it a more effective tool for the detection and degradation monitoring of environmental MNPs. Moreover, applying this PIERS-based method to real-world environmental samples represents an important next step, as such matrices typically contain organic matter, ions, and other coexisting contaminants that may affect substrate performance or interfere with spectral acquisition.

Conflicts of interest

There are no conflicts to declare.

Data availability

Data that support the findings of this study are available from the corresponding author upon reasonable request.

The supplementary information includes: synthesis reaction for flower-like Ag nanoflakes (NFs), schematic illustration of the synthesis process for micro- and nano-sized PVC plastics, SEM images of PVC powder, synthesized PVC, and UV-irradiated Ag NF-TiO_2 substrate loaded with PVC-MNPs, Raman, SERS, and PIERS spectra, water contact angle (WCA) analysis, XPS and ATR-FTIR spectra, enhancement factor (EF) calculations, and a comparative review of detection techniques for micro- and nanoplastics (MNPs). See DOI: **https://doi.org/10.1039/d5ta03860j**.

Acknowledgements

O. Ayeni wishes to thank the Petroleum Technology Development Fund (PTDF) for providing funding for his doctoral studies. This work is financially supported by the Deutsche Forschungsgemeinschaft (DFG, German Research Foundation) Heisenberg Programme – Project AM 519/4-1 and Deutsche Forschungsgemeinschaft (DFG, German Research Foundation) Individual Research Grants (project number 448935424 – project FA 234/35-1).

References

1 J. Miliute-Plepiene, A. Fråne and A. M. Almasi, *Clean Eng. Technol.*, 2021, **4**, 100246.
2 L. Bernard, D. Bourdeaux, B. Pereira, N. Azaroual, C. Barthélémy, C. Breysse, P. Chennell, R. Cueff, T. Dine, T. Eljezi, F. Feutry, S. Genay, N. Kambia, M. Lecoeur, M. Masse, P. Odou, T. Radaniel, N. Simon, C. Vaccher, C. Verlhac, M. Yessad, B. Décaudin and V. Sautou, *Talanta*, 2017, **162**, 604–611.
3 Microplastics are everywhere — we need to understand how they affect human health, *Nat. Med.*, 2024, **30**, 913, DOI: **10.1038/s41591-024-02968-x**.
4 M. Kozlov, *Nature*, 2024, DOI: **10.1038/D41586-024-00650-3**.
5 E. Dube and G. E. Okuthe, *Int. Res. J. Publ. Environ. Health*, 2023, 6667, DOI: **10.3390/IJERPH20176667**.
6 A. O. Nosova and M. V. Uspenskaya, *Environ. Adv.*, 2023, **13**, 100437.
7 A. Turner and M. Filella, *Environ. Sci.: Processes Impacts*, 2021, **23**, 1376–1384.
8 X. Ruan, L. Xie, J. Liu, Q. Ge, Y. Liu, K. Li, W. You, T. Huang and L. Zhang, *J. Hazard. Mater.*, 2024, 132702, DOI: **10.1016/J.JHAZMAT.2023.132702**.
9 V. Menon, S. Sharma, S. Gupta, A. Ghosal, A. K. Nadda, R. Jose, P. Sharma, S. Kumar, P. Singh and P. Raizada, *Chemosphere*, 2023, 137848, DOI: **10.1016/J.CHEMOSPHERE.2023.137848**.
10 R. Yin, H. Ge, H. Chen, J. Du, Z. Sun, H. Tan and S. Wang, *Environ. Adv.*, 2021, **5**, 100096.
11 L. Yerid Vélez-Escamilla, F. F. Contreras-Torres, L. Y. Vélez-Escamilla and F. F. Contreras-Torres, *Part. Part. Syst. Char.*, 2022, **39**, 2100217.
12 L. R. Terry, S. Sanders, R. H. Potoff, J. W. Kruel, M. Jain and H. Guo, *Anal. Sci. Adv.*, 2022, **3**, 113–145.

13 W. J. Peveler, S. Ben Jaber and I. P. Parkin, *Forensic Sci., Med., Pathol.*, 2017, **13**, 490–494.
14 J. M. Chalmers, H. G. M. Edwards and M. D. Hargreaves, *Infrared and Raman Spectroscopy in Forensic Science*, 2012, DOI: 10.1002/9781119962328.
15 K. A. Prokhorov, D. A. Aleksandrova, E. A. Sagitova, G. Y. Nikolaeva, T. V. Vlasova, P. P. Pashinin, C. A. Jones and S. J. Shilton, *J. Phys.: Conf. Ser.*, 2016, **691**, DOI: 10.1088/1742-6596/691/1/012001.
16 M. Baibarac, L. Stingescu, M. Stroe, C. Negrila, E. Matei, L. C. Cotet, I. Anghel, I. E. Şofran and L. Baia, *Polymers*, 2021, **13**, 1–16.
17 S. Ben-Jaber, W. J. Peveler, R. Quesada-Cabrera, E. Cortés, C. Sotelo-Vazquez, N. Abdul-Karim, S. A. Maier and I. P. Parkin, *Nat. Commun.*, 2016, **7**, DOI: 10.1038/ncomms12189.
18 Q. D. Mai, H. A. Nguyen, T. L. H. Phung, N. Xuan Dinh, Q. H. Tran, T. Q. Doan, A. T. Pham and A. T. Le, *ACS Appl. Nano Mater.*, 2022, **5**, 15518–15530.
19 M. Zhang, H. Sun, X. Chen, J. Yang, L. Shi, T. Chen, Z. Bao, J. Liu and Y. Wu, *ACS Sens.*, 2019, **4**, 1670–1681.
20 S. Y. Huang, W. N. Gao, C. M. Chou and V. K. S. Hsiao, *RSC Adv.*, 2023, **13**, 15634–15639.
21 D. Glass, E. Cortés, S. Ben-Jaber, T. Brick, W. J. Peveler, C. S. Blackman, C. R. Howle, R. Quesada-Cabrera, I. P. Parkin and S. A. Maier, *Adv. Sci.*, 2019, **6**(22), 1–10, DOI: 10.1002/advs.201901841.
22 C. Zhan, X. J. Chen, J. Yi, J. F. Li, D. Y. Wu and Z. Q. Tian, *Nat. Rev. Chem.*, 2018, **2**(9), 216–230.
23 G. Barbillon, *Photonics*, 2022, **9**, 1–9, DOI: 10.3390/photonics9080562.
24 J. Ye, R. Arul, M. K. Nieuwoudt, J. Dong, T. Zhang, L. Dai, N. C. Greenham, A. Rao, R. L. Z. Hoye, W. Gao and M. C. Simpson, *J. Phys. Chem. Lett.*, 2023, 4607–4616.
25 V. Tan Tran, M. Phuong Le, N. Hai Pham, T. Hai Yen Le, V. Tuyen Nguyen, T. Hong Pham, T. San Nguyen, Q. Hoa Nguyen, V. Thanh Pham, T. Tam Nguyen, C. Toan Nguyen, A. Bang Ngac, O. Martínez Sacristán and T. Ha Tran, *Appl. Surf. Sci.*, 2024, **657**, 159785, DOI: 10.1016/j.apsusc.2024.159785.
26 M. Zhang, T. Chen, Y. Liu, J. Zhu, J. Liu and Y. Wu, *ChemNanoMat*, 2019, **5**, 55–60.
27 J. Shondo, S. Veziroglu, T. Tjardts, T. Bin Sarwar, Y. K. Mishra, F. Faupel and O. C. Aktas, *Small*, 2022, **18**, DOI: 10.1002/smll.202203861.
28 T. Tjardts, M. Elis, J. Shondo, L. Voß, U. Schürmann, F. Faupel, L. Kienle, S. Veziroglu and O. C. Aktas, *ChemSusChem*, 2024, **17**, DOI: 10.1002/cssc.202400046.
29 Z. Zhu, K. Han, Y. Feng, Z. Li, A. Zhang, T. Wang, M. Zhang and W. Zhang, *ACS Appl. Mater. Interfaces*, 2023, **15**, 36988–36998.
30 W. Hamd, E. A. Daher, T. S. Tofa and J. Dutta, *Front. Mar. Sci.*, 2022, **9**, DOI: 10.3389/fmars.2022.885614.
31 Y. He, A. U. Rehman, M. Xu, C. A. Not, A. M. C. Ng and A. B. Djurišić, *Heliyon*, 2023, **9**, e22562.
32 K. J. Ramírez-Escárcega, K. J. Amaya-Galván, J. C. García-Prieto, F. De, J. Silerio-Vázquez and J. B. Proal-Nájera, *J. Environ. Chem. Eng.*, 2025, **13**, 115594, DOI: 10.1016/j.jece.2025.115594.
33 A. Chamas, H. Moon, J. Zheng, Y. Qiu, T. Tabassum, J. Hee Jang, M. Abu-Omar, S. L. Scott and S. Suh, *ACS Sustainable Chem. Eng.*, 2020, **8**, 3511.
34 A. Beltrán-Sanahuja, N. Casado-Coy, L. Simó-Cabrera and C. Sanz-Lázaro, *Environ. Pollut.*, 2020, **259**, 113836.
35 Y. Hibi, T. Matsumoto, M. Midorikawa, S. Uesaka, M. Mizoshiri, T. Tanimura, M. Okada, K. Naito and M. Naito, *Polym. Degrad. Stab.*, 2025, **232**, 111128, DOI: 10.1016/j.polymdegradstab.2024.111128.
36 S. Kumari, D. Yadav, S. Yadav, M. Selvaraj, G. Sharma, A. Karnwal and S. Yadav, *Polym. Degrad. Stab.*, 2025, **233**, 111174.
37 J. Shondo, S. Veziroglu, T. Tjardts, J. Fiutowski, S. Schröder, Y. K. Mishra, T. Strunskus, H. G. Rubahn, F. Faupel and O. C. Aktas, *Adv. Mater. Interfaces*, 2022, 2102126, DOI: 10.1002/admi.202102126.
38 S. Veziroglu, M. Z. Ghori, M. Kamp, L. Kienle, H. G. Rubahn, T. Strunskus, J. Fiutowski, J. Adam, F. Faupel and O. C. Aktas, *Adv. Mater. Interfaces*, 2018, 1800465, DOI: 10.1002/ADMI.201800465.
39 Z. Khoryani, J. Seyfi and M. Nekoei, *Appl. Surf. Sci.*, 2018, **428**, 933–940.
40 K. Bi, M. Huang, Z. Ning, Z. Dian zi xue hui, Electronic Manufacturing & Packaging Technology Society, D. Li gong da xue, Institute of Electrical and Electronics Engineers and P. & M. T. S. Components, *2013 14th International Conference on Electronic Packaging Technology (ICEPT 2013),* Dalian, China, August 11∼14, 2013.
41 S. Y. Zhao, X. Li, Y. H. Mei and G. Q. Lu, *J. Mater. Sci.: Mater. Electron.*, 2016, **27**, 10941–10950.
42 M. Kerker, O. Siiman, L. A. Bumm and D.-S. Wang, *Appl. Opt.*, 1980, **19**, 3253–3255, DOI: 10.1364/AO.19.003253.
43 O. Arjmandi-Tash, N. M. Kovalchuk, A. Trybala, I. V Kuchin and V. Starov, *Langmuir*, 2017, **33**, 4367–4385, DOI: 10.1021/acs.langmuir.6b04094.
44 B. Gady, D. Schleef, R. Reifenberger, D. Rimai and L. DeMejo, *Phys. Rev. B: Condens. Matter Mater. Phys.*, 1996, **53**, 8065–8070.
45 J. Langer, D. Jimenez de Aberasturi, J. Aizpurua, R. A. Alvarez-Puebla, B. Auguie, J. J. Baumberg, G. C. Bazan, S. E. J Bell, A. Boisen, A. G. Brolo, J. Kneipp, N. A. Kotov, H. Kuang, E. C. Le Ru, H. Kwee Lee, J.-F. Li, X. Yi Ling, S. A. Maier, T. Mayerho, M. Moskovits, K. Murakoshi, J.-M. Nam, S. Nie, Y. Ozaki, I. Pastoriza-Santos, J. Perez-Juste, J. Popp, A. Pucci, S. Reich, B. Ren, G. C. Schatz, T. Shegai, S. Schlu, L.-L. Tay, K. George Thomas, Z.-Q. Tian, R. P. Van Duyne, T. Vo-Dinh, Y. Wang, K. A. Willets, C. Xu, H. Xu, Y. Xu, Y. S. Yamamoto, B. Zhao and L. M. Liz-Marza, *ACS Nano*, 2020, **14**, 28–117, DOI: 10.1021/acsnano.9b04224.
46 D. Glass, E. Cortés, S. Ben-Jaber, T. Brick, W. J. Peveler, C. S. Blackman, C. R. Howle, R. Quesada-Cabrera, I. P. Parkin, S. A. Maier, S. A. Maier, D. Glass, S. Ben-Jaber, W. J. Peveler, C. S. Blackman, R. Quesada-Cabrera,

I. P. Parkin, E. Cortés and C. R. Howle, *Adv. Sci.*, 2019, 1901841, DOI: 10.1002/advs.201901841.
47 M. Zhang, T. Chen, Y. Liu, J. Zhu, J. Liu and Y. Wu, *ChemNanoMat*, 2019, **5**, 55–60.
48 S. M. Kuznetsov, E. A. Sagitova, K. A. Prokhorov, G. Y. Nikolaeva, D. I. Mendeleev, P. Donfack and A. Materny, *Spectrochim. Acta, Part A*, 2021, 119494, DOI: 10.1016/j.saa.2021.119494.
49 V. Ludwig, Z. M. Da Costa Ludwig, M. M. Rodrigues, V. Anjos, C. B. Costa, D. R. Sant'Anna das Dores, V. R. da Silva and F. Soares, *Vib. Spectrosc.*, 2018, **98**, 134–138.
50 Y. Luo, M. Al Amin, C. T. Gibson, C. Chuah, Y. Tang, R. Naidu and C. Fang, *Environ. Pollut.*, 2022, **298**, 118857.
51 D. Glass, E. Cortés, W. J. Peveler, C. R. Howle, R. Quesada-Cabrera, I. P. Parkin and S. A. Maier, *Proc. SPIE*, 2020, **11416**, 1141602, DOI: 10.1117/12.2557517.
52 W. Zhang, Z. Fang and X. Zhu, *Chem. Rev.*, 2017, **117**, 5095–5109, DOI: 10.1021/acs.chemrev.6b00337.
53 C. Fang, Z. Sobhani, X. Zhang, C. T. Gibson, Y. Tang and R. Naidu, *Water Res.*, 2020, **183**, 116046.
54 Q.-D. Mai, D. Thi, H. Trang, T. N. Bach, V. T. Le Na, A.-T. Pham and A.-T. Le, *RSC Adv.*, 2025, **15**, 4149–4162, DOI: 10.1039/d4ra07718k.
55 J. Qin, S. Zeng, X. Wang and C. Lin, *Chemosphere*, 2022, **299**, 134399.
56 V. S. Solodovnichenko, V. A. Polyboyarov, A. A. Zhdanok, A. B. Arbuzov, E. S. Zapevalova, Y. G. Kryazhev and V. A. Likholobov, in *Procedia Engineering*, Elsevier Ltd, 2016, vol. 152, pp. 747–752.
57 B. Gewert, M. M. Plassmann and M. Macleod, *Environ. Sci.: Processes Impacts*, 2015, **17**, 1513–1521, DOI: 10.1039/c5em00207a.
58 M. C. Celina, E. Linde and E. Martinez, *Polym. Degrad. Stab.*, 2021, **188**, 109550.
59 J. Song, J. Wang, J. Sima, Y. Zhu, X. Du, P. T. Williams and Q. Huang, *Chemosphere*, 2023, **338**, 139535, DOI: 10.1016/j.chemosphere.2023.139535.
60 N. Sazali, H. Ibrahim, A. S. Jamaludin, M. A. Mohamed, W. N. W. Salleh and M. N. Z. Abidin, *IOP Conf. Ser. Mater. Sci. Eng.*, 2020, **788**, 012048.
61 M. M. Caruso, D. A. Davis, Q. Shen, S. A. Odom, N. R. Sottos, S. R. White and J. S. Moore, *Chem. Rev.*, 2009, **109**, 5755–5798, DOI: 10.1021/cr9001353.
62 T. Abdul-kader Saleh, A. Shihab Ahmed, A. K. Hussein, S. Ghosh, S. Kommanaboyina and M. H. Al-Mashhadani, *J. Polym. Res.*, 2024, **31**, DOI: 10.1007/s10965-024-03887-8.
63 Q. Zhang, J. Ge, T. Pham, J. Goebl, Y. Hu, Z. Lu and Y. Yin, *Angew. Chem., Int. Ed.*, 2009, **48**, 3516–3519.
64 Y.-Y. Zhao, X.-L. Ren, M.-L. Zheng, F. Jin, J. Liu, X.-Z. Dong, Z.-S. Zhao and X.-M. Duan, *Opto-Electron. Adv.*, 2021, **4**, 200101, DOI: 10.29026/oea.2021.200101.
65 G. Kumari, R. Kamarudheen, E. Zoethout and A. Baldi, *ACS Catal.*, 2021, **11**, 3478–3486.
66 C. Zhang, J. Qi, Y. Li, Q. Han, W. Gao, Y. Wang, J. Dong, A. B. Evlyukhin, Y. Kim, C. Zhang, J. Qi, Y. Li, Q. Han, W. Gao, Y. Wang and J. Dong, *Nanomaterials*, 2022, **12**, 1329, DOI: 10.3390/nano12081329.
67 L. V. Bora, M. Bhatt, A. Patel and N. V. Bora, *Plastic Degradation by Photocatalysis: Basic Concepts and General Mechanisms*, 2024, DOI: 10.1021/bk-2024-1489.ch001.
68 E. Kinyua, G. Nyakairu, E. Tebandeke and N. Odume, *Adv. Environ. Eng. Res.*, 2023, **04**, 1–21.
69 S. Veziroglu, M. Ullrich, M. Hussain, J. Drewes, J. Shondo, T. Strunskus, J. Adam, F. Faupel and O. C. Aktas, *Surf. Coat. Technol.*, 2020, 125613, DOI: 10.1016/j.surfcoat.2020.125613.